SANDIA REPORT
SAND20XX-XXXX
Printed Click to enter a date

Sandia National Laboratories

Effect of Microstructural Bands on the Localized Corrosion of Laser Surface-melted 316L Stainless Steel

Yoon Hwa*,*** Christopher S. Kumai, * Nancy Yang, ** Joshua K. Yee** and Thomas M. Devine‡,*

‡Corresponding author. E-mail: devine@berkeley.edu

* Department of Materials Science and Engineering, University of California, Berkeley, CA, USA, 94720

** Sandia National Laboratory, Livermore, CA, USA, 94550.

*** Present address: School of Electrical, Computer and Energy Engineering, Arizona State University, Tempe, AZ, USA, 85281

Prepared by
Sandia National Laboratories
Albuquerque, New Mexico
87185 and Livermore,
California 94550

Issued by Sandia National Laboratories, operated for the United States Department of Energy by National Technology & Engineering Solutions of Sandia, LLC.

Available to DOE and DOE contractors from
U.S. Department of Energy
Office of Scientific and Technical Information
P.O. Box 62
Oak Ridge, TN 37831

Telephone: (865) 576-8401
Facsimile: (865) 576-5728
E-Mail: reports@osti.gov
Online ordering: http://www.osti.gov/scitech

Available to the public from
U.S. Department of Commerce
National Technical Information Service
5301 Shawnee Rd
Alexandria, VA 22312

Telephone: (800) 553-6847
Facsimile: (703) 605-6900
E-Mail: orders@ntis.gov
Online order: https://classic.ntis.gov/help/order-methods/

ABSTRACT

The localized corrosion of laser surface melted (LSM) 316L stainless steel is investigated by a combination of potentiodynamic anodic polarization in 0.1M HCl and microscopic investigation of the initiation and propagation of localized corrosion. The pitting potential of LSM 316L is significantly lower than the pitting potential of wrought 316L. The LSM microstructure is highly banded as a consequence of the high laser power density and high linear energy density. The bands are composed of zones of changing modes of solidification, cycling between very narrow regions of primary austenite solidification and very wide regions of primary ferrite solidification. Pits initiate in the outer edge of each band where the mode of solidification is primary austenite plane front solidification and primary austenite cellular solidification. The primary austenite regions have low chromium concentration (and possibly low molybdenum concentration), which explains their susceptibility to pitting corrosion. The ferrite is enriched in chromium, which explains the absence of pitting in the primary ferrite regions. The presence of the low chromium regions of primary austenite solidification explains the lower pitting resistance of LSM 316L relative to wrought 316L. The influence of banding on localized corrosion is applicable to other rapidly solidified processes such as additive manufacturing.

KEY WORDS: Corrosion, Laser additive manufacturing, microstructural bands, Stainless Steel.

ACKNOWLEDGEMENTS

We are grateful to the Molecular Foundry and National Center of Electron Microscopy at the Lawrence Berkeley National Laboratory for the use of the Zeiss Gemini Ultra-55 analytical scanning electron microscope, the Bruker AXS D8 Discover GADDS X-ray diffractometer, the FIB Strata, the Nano Mill and the FEI TitanX 60-300. Work at the Molecular Foundry was supported by the Office of Science, Office of Basic Energy Sciences, of the U.S. Department of Energy under contract no. DE-AC02-05CH11231.

Our research was made possible by the programmatic support of Dr. Andy Vance.

This paper describes objective technical results and analysis. Any subjective views or opinions that might be expressed in the paper do not necessarily represent the views of the U.S. Department of Energy or the United States Government.

CONTENTS

LIST OF FIGURES

This page left blank

ACRONYMS AND DEFINITIONS

Abbreviation	Definition
AM	additive manufacturing
CS	cellular solidification
DED	Directed Energy Deposition
EDS	equiaxed dendritic solidification
FIB	Focused Ion Beam
LED	linear energy density
LPBF	Laser Powder Bed Fusion
LPD	laser power density
LSM	laser surface-melting
PFS	plane front solidification
RHE	reversible hydrogen electrode
SA	solution annealing
SEM	scanning electron microscope
SS	stainless steel
TEM	Transmission Electron Microscope
UHP	ultra-high purity

1. INTRODUCTION

Our recent paper[1] compares the microstructures of directed energy deposition additively manufactured (DED-AM) 316L stainless steel (SS) and of laser surface-melted (LSM) 316L SS. The microstructure within each hatch of an additively manufactured 316L SS cylinder is the same as that within a single track formed by linearly translating a plate beneath a stationary laser beam. Single tracks are therefore used to investigate the influence of laser beam power and translation speed on microstructure.[1]

It is well known that high laser power density (LPD) and high linear energy density (LED) are beneficial in completely melting the powder and creating high density deposits.[2]-[4] However, too high values of LPD and LED cause voids and changes in composition caused by different rates of vaporization of different elements.[4]-[6] In addition, high values of LPD and LED affect the microstructure of LSM deposits and additive manufactured (AM)components.[1] In the present paper we consider high values of LPD and LED that are not high enough to create voids and significant vaporization-induced changes in composition and instead focus on the microstructures associated with high LPD and LED.

Figure 1a shows that the microstructures of hatches and tracks of 316L SS formed with relatively high LPD and high LED are significantly inhomogeneous, which raises concerns about local variations in mechanical properties[3], [4] and of other microstructure-sensitive properties such as corrosion resistance. The distinctive features of the microstructure's inhomogeneous character are two types of bands that are revealed by metallographic etching. "Solidification bands" are so named because they form the interface between the surface melted track and the substrate, and the interface between adjacent hatches and because their mode of solidification is different from the solidification mode of the bulk of the laser melted track/hatch.[1] A second type of band, called "convection bands," form within hatches/tracks as a result of high values of LPD and LED. [1] The convection bands appear as concentric, quasi circular arcs in the cross-section of a hatch/track (Figure 1a) and form half-circular ripples on the free surface of a hatch/track (Figure 1b).

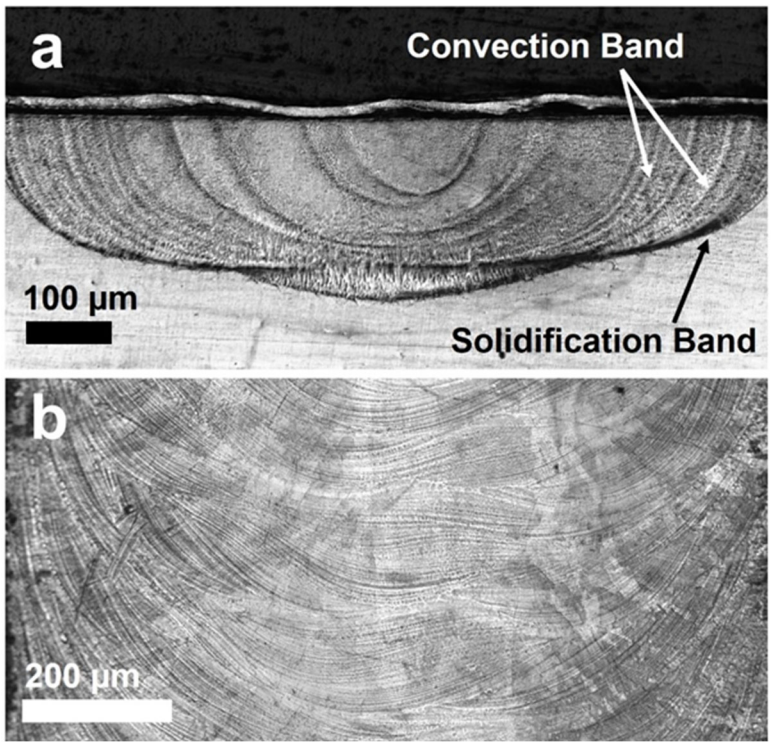

Figure 1. (a)Cross section of laser remelted track formed in plate of 316L SS with a laser power of 307 W and a translation speed of 5 mm/s. Potentiostatic etch in concentrated nitric acid. (b) Surface ripples visible in the optical micrograph of the top surface of laser surface melted track formed on a plate of 316L SS with a laser power of 307 W and a translation speed of 5 mm/s.

Convection bands are the result of convection induced in the melt at high values of LPD and LED by a combination of the Marangoni effect and, especially, a high recoil pressure,[7] and the number of convection bands increases with increasing LPD and LED. [1] The convection sweeps away the liquid at the liquid-solid interface and thereby replaces the solute-enriched interfacial liquid layer (if the solute's equilibrium partition coefficient, k, is less than 1) or solute impoverished interfacial liquid layer (if k is greater than 1) with the composition of the bulk liquid. The abrupt change in composition of the interfacial liquid (as well as possible abrupt changes in interfacial undercooling and cooling rate) generate the abrupt changes in the mode of solidification and in the composition of the just-frozen solid, which are responsible for the differential etching that reveals the convection bands. The details of the changes in composition and in mode of solidification associated with convection bands are only apparent at high magnifications and are presented in the Results section of this paper.

It is possible that changes in mode of solidification associated with banding in LSM tracks and in AM hatches can affect the corrosion resistance. The corrosion behavior of a number of AM alloys is reviewed in a recent article.[8] The results of a number of individual studies of corrosion of AM 316L stainless steel are described in the Discussion. In the present paper we investigate the localized corrosion of LSM 316L SS. The results reveal the influence of banding on the susceptibility to pitting corrosion.

2. EXPERIMENTAL PROCEDURES

The surface of a plate of 316L SS was remelted by linearly translating the plate under a stationary, perpendicularly incident laser beam. The speed of translation is 5 mm/s and the power of the laser is 187 W. Figure 2 shows approximately three of a total of approximately 100, parallel, partially overlapping, laser melted tracks that cover the sample's surface. Each track is approximately 250 μm wide and 2 cm long and the total area of melting is 2 cm X 2 cm. The LSM was performed inside a glove-box that contains an Aerotech XY-translation stage and a welding head (IPG Model P30-002417-V4A1A) of a 500W IPG YLR-500-AC-Y14 fiber laser (1.07 μm). The atmosphere inside the glovebox is stagnant ultra-high purity grade (UHP) argon. The diameter of the laser beam at the 100 mm focal length lens is 13 mm and the calculated radius (e^{-1}) of the focused Gaussian beam is approximately 10 μm. Given the surface roughness and slight curvature of the 316L SS plate, we estimate that the laser spot on the plate's surface is within ± 1.5 mm above/below the focal spot so that the radius of the laser beam on the sample's surface is in the range of 10 μm to 13 μm. Based on laser beam radii of 10 μm and 13 μm, and assuming the ratio of absorbed laser intensity to incident laser intensity is 0.3,[9],[10] the values of the main processing parameters are LPD and LED equal 17.9 MW/cm^2 and 37.5 MJ/cm, and 10.6 MW/cm^2 and 22.2 MJ/cm, respectively.

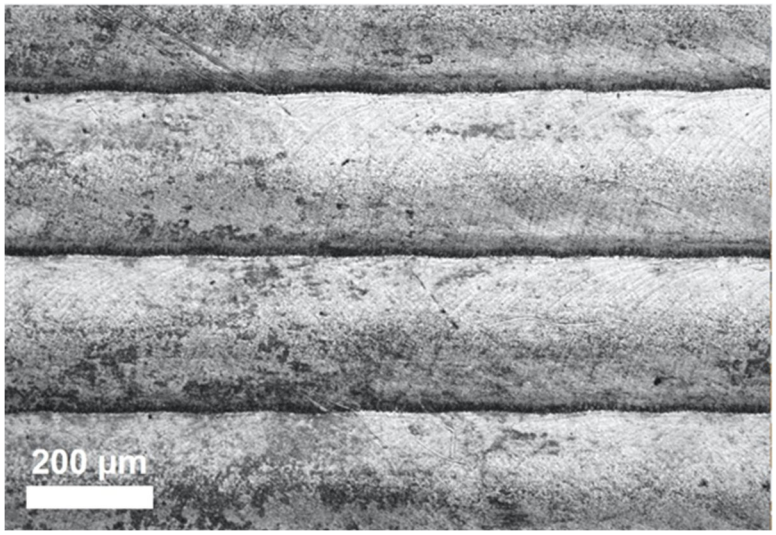

Figure 2. As-laser-melted surface of 316L SS with partially overlapping tracks formed with an incident laser power of 187 W and a translation speed of 5 mm/s.

The LSM tracks were first examined in an optical microscope and then in a scanning electron microscope. Next, the top surface and the cross-sectional surface of the LSM were ground, polished, etched and their microstructure was examined with an optical microscope.

The etching procedure used to investigate the microstructure consisted of anodic polarization in concentrated nitric acid (68 w/o – 69 w/o, Fisher Scientific) for 10 s at a potential of +0.8V vs a platinum electrode, which serves as both a counter electrode and as a pseudo-reference electrode.

High resolution energy-dispersive analysis was conducted on samples of a LSM track in an effort to determine the spatial variation of the alloy's composition. The measurements were obtained with an FEI TitanX-60-300 microscope. The Transmission Electron Microscope (TEM) sample was prepared by focused ion beam (Focused Ion Beam (FIB), FEI Strata 235) lift out technique which is followed by nano milling (Fischione nano mill) to obtain desired sample thickness.

The corrosion behavior of the plate of wrought 316L SS and of the LSM 316L SS is investigated by potentiodynamic anodic polarization in UHP nitrogen-saturated 0.1M HCl at room temperature. The tests were conducted in a glass cell with approximately 0.5 liter of solution. The samples were polarized with the aid of a potentiostat (Biologic VSP) at a rate of 1 mV/s. The sample's potential is measured with respect to a saturated calomel reference electrode and is reported versus a reversible hydrogen electrode (RHE).

Samples for polarization tests were prepared by first grinding and polishing the surface. Next, the test area of the sample was created by coating the untested area with Glyptal, which is an electrically insulating paint. After the polarization test, the Glyptal paint was removed by acetone, followed by immediate rinsing with highly purified water

The influence of microstructure on the initiation of localized corrosion is investigated by examining in an optical microscope and a scanning electron microscope (Zeiss Zemini Ultra 55) the surfaces of samples that are slightly etched after their local corrosion in the potentiodynamic anodic polarization tests.

3. RESULTS

Our initial tests were conducted on as-laser-melted surfaces without any additional preparation. The results, which are presented in Appendix B, indicate that topography of the as-melted surface has a dominant effect on initiation of localized corrosion and the surface topography masks the influence of microstructure. While the influence of surface topography is important, the focus of our paper is the influence of microstructure. Accordingly, the results of surface topography are presented in Appendix B and the balance of this paper discusses the results of anodic polarization tests of metallographically polished surfaces of the plate of wrought 316L SS and of the laser surface-melted (LSM) 316L SS.

3.1. Ground and Polished Surfaces of 316L SS Plate and Laser Surface Melted 316L SS

Figure 3 compares the anodic polarization behavior of the ground and polished surface of the plate of wrought 316L SS and of the ground and polished LSM 316L SS surface. The polarization behavior of both the top surface and of the cross-sectional surface of the LSM layer are similar and the LSM 316L SS exhibits a significantly lower pitting potential (-0.4 V) compared to that of the wrought 316L plate (0 V). Comparison of the results presented in Figure 3 indicates grinding and polishing increases the pitting potential of the plate of the wrought 316L SS but decreases the pitting potentials of the LSM 316L SS. Although their breakdown potentials are similar, different types of localized corrosion occur on the polished top surface and cross-sectional surface of the LSM 316L SS. We first describe the localized corrosion of the polished top surface.

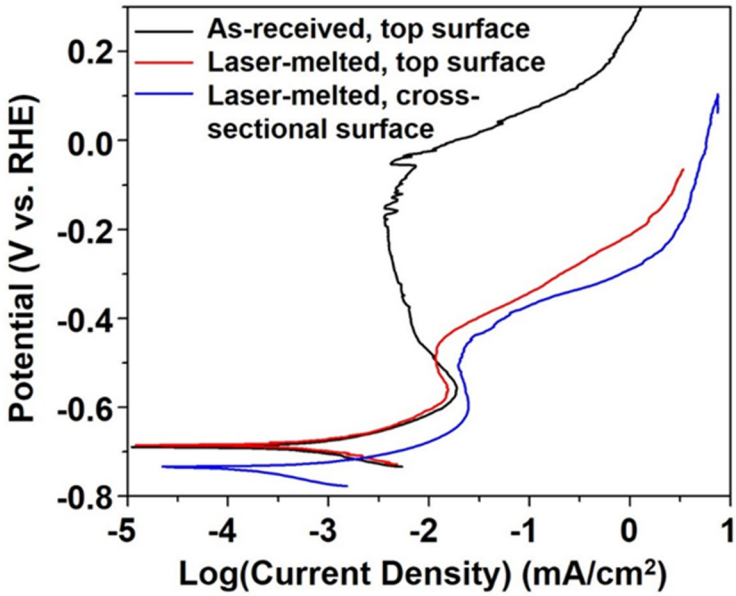

Figure 3. Polarization curves in N2-saturated 0.1M HCl of ground and polished surfaces; (1) wrought 316L plate, (2) top surface of LSM 316L SS, and (3) cross-section surface of LSM 316L SS.

3.2. Top Surface of Laser Surface Melted 316L SS – Nucleation of Pitting Corrosion

As is the case in most, if not all, earlier studies quasi-circular pits occur at random on the surface of the polished, wrought plate of 316L. In contrast, as shown in Figure 4a, the pits on the polished, top surface of the LSM 316L SS have a distinctive, non-circular shape. Light etching after anodic polarization (Figure 4b) indicates the pits occur at specific locations in the microstructure and the shapes of the pits are influenced by the microstructure. Pits are seen to nucleate along the outer perimeter of the convection bands (Figure 4b). The location of pit nucleation is further revealed by the combination of the optical micrograph (Figure 5a) and the scanning electron micrographs (Figure 5b and c) of the same region of a sample that was lightly etched after anodic polarization.

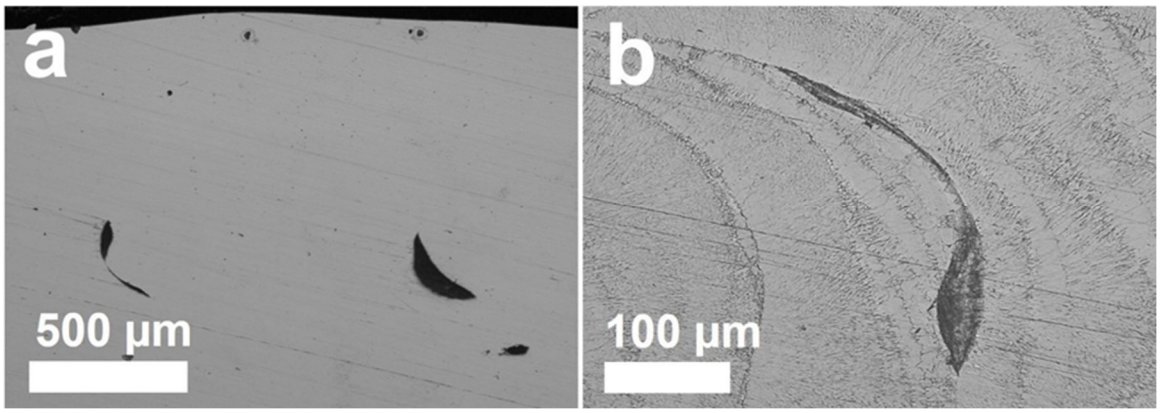

Figure 4. Ground and polished top surface of the LSM 316L SS. (a) after anodic polarization in 0.1M HCl, and (b) after anodic polarization in 0.1M HCl and slight etching in concentrated nitric acid.

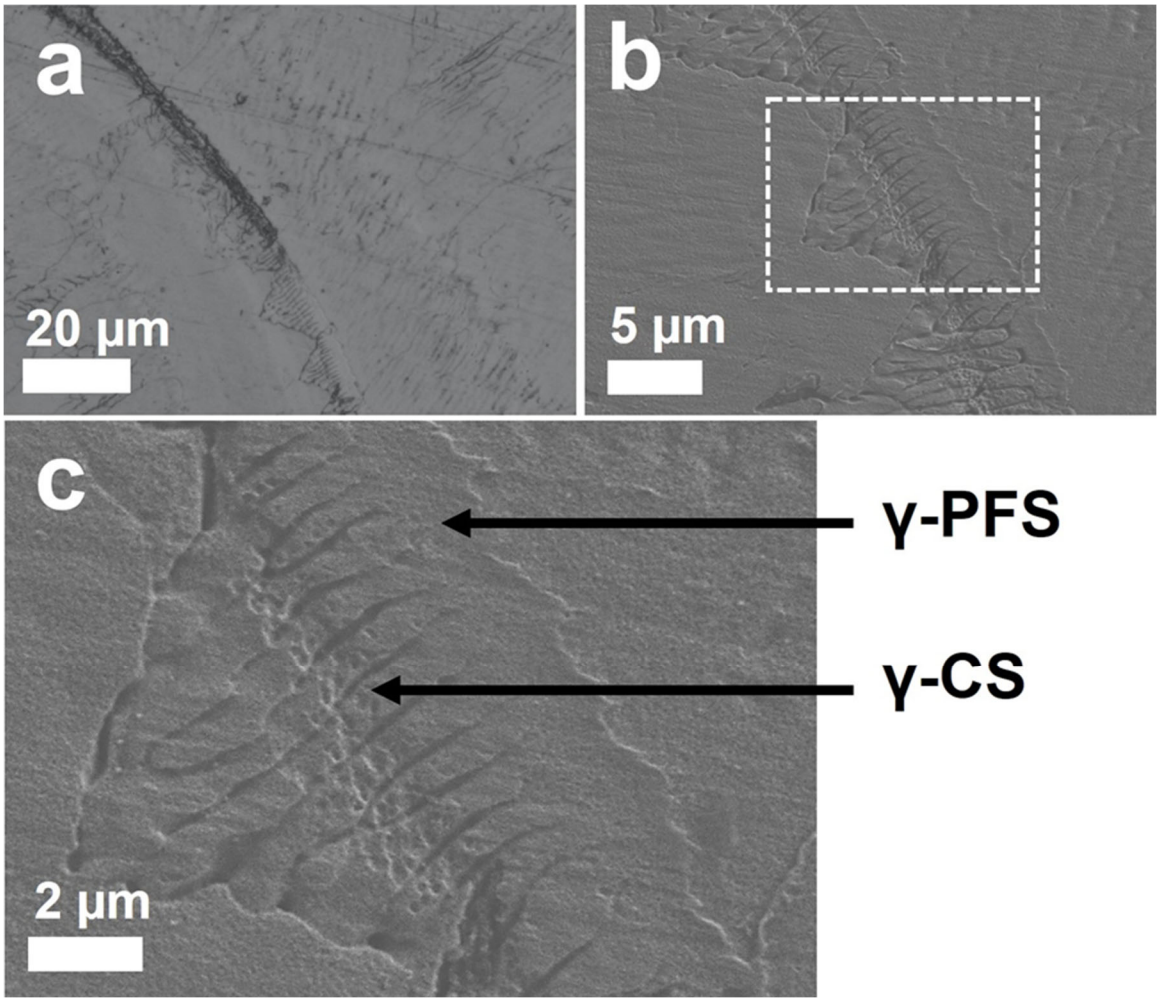

Figure 5. Ground and polished top surface of laser melted 316L SS anodically polarized in 0.1 M HCl and slightly etched in concentrated nitric acid. Combination of (a) optical micrograph, and (b) scanning electron micrographs (SEM) at site of localized corrosion along the outer edge of a convection band, which is revealed by the slight etching. (c) High magnification SEM image of the marked area in Figure 5b. The two modes of primary austenite solidification are labeled in the high magnification SEM.

As discussed in Appendix A, potentiostatic etching in concentrated nitric acid preferentially attacks the regions of high chromium concentration. The preferential etching is a consequence of the oxidation of Cr^{+3} to Cr^{+6}, which is highly soluble. In Figure 5c the light etching indicates the initial mode of solidification along the extreme outer edge of the convection band is plane front solidification (PFS) and its smaller degree of etching indicates a lower chromium concentration, which indicates the primary phase of solidification is austenite, γ. The solidification microstructure is labeled γ-PFS. At a short distance in from the outer edge the mode of solidification changes to cellular (CS) with preferential etching of Cr-rich cell boundaries, which indicates the primary phase of solidification is austenite, γ. Here the solidification microstructure is designated γ-CS.

Ferrite is the thermodynamically stable primary phase of solidification of 316L SS and austenite is the thermodynamically metastable primary phase. [11]-[14] The initial freezing as PFS of the metastable austenite phase (γ-PFS) followed by austenitic cellular solidification (γ-CS) occurs as a result of the high cooling rate and high undercooling at the outer edge of the convection band. [1] The change

from plane front solidification to cellular solidification is the result of transitioning from transient to steady-state conditions[15] and/or a consequence of the decrease in G/V (= thermal gradient in the liquid at the liquid-solid interface divided by the velocity of the liquid-solid interface) with increasing distance from the fusion line.[16]-[18] The SEM in Figure 5c of the lightly etched, pitted sample shows that submicron diameter pits (approx. 0.2 μm) nucleate within the cores of the austenite cells. In addition, the SEMs in Figure 6a and b of the lightly etched, pitted sample show submicron diameter pits in both the γ-PFS region as well as in the austenite cores of the γ-CS region. The diameter of the solidification cells is approximately 1 μm, which is clearly larger than the 0.2 μm diameter of the tiny pits that appear homogeneously distributed throughout the interior of the cell (Figure 5c and Figure 6b). Additional TEM work, which is outside the scope of the current investigation, is required in order to determine if there is a microstructural cause of the 0.2 μm scale of the pits.

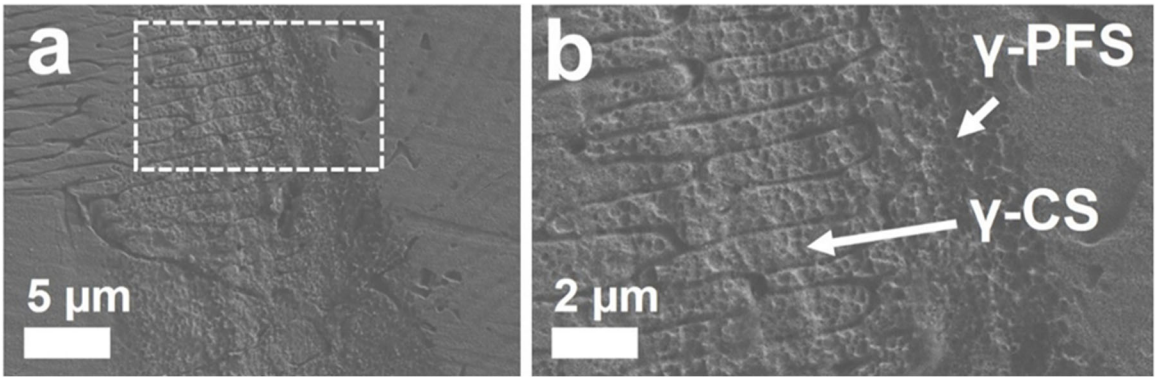

Figure 6. Ground and polished top surface of LSM 316L SS anodically polarized in 0.1M HCl and slightly etched in concentrated nitric acid. SEM images of site of pit initiation along the outer edge of a convection band in the γ-PFS and γ-CS regions.

Significant changes in the microstructure occur with increasing distance from the two narrow regions of primary austenite solidification (i.e., γ-PFS and γ-CS) that occur along the outer edge of the convection band. The changes in microstructure consist of changes in the primary phase of solidification and changes in the mode of solidification. However, pits do not initiate in any of these regions. Since pitting corrosion is the primary focus of this paper the additional changes in microstructure are presented and discussed in an appendix (Appendix C).

The entire microstructure is composed of a series of convection bands and the microstructure within each band is summarized in the sketch presented in Figure 7. Starting at the outer edge of the convection band the initial solidification occurs as γ-PFS followed by γ-CS. Next, as discussed in Appendix C, there is a transition from γ-CS to α-CS followed by a transition from α-CS to α–equiaxed dendritic solidification. Although the regions of primary austenite solidification are very small compared to the relatively large regions of primary ferrite solidification, the regions of primary austenite solidification are very important as they are the sites where pits are nucleated.

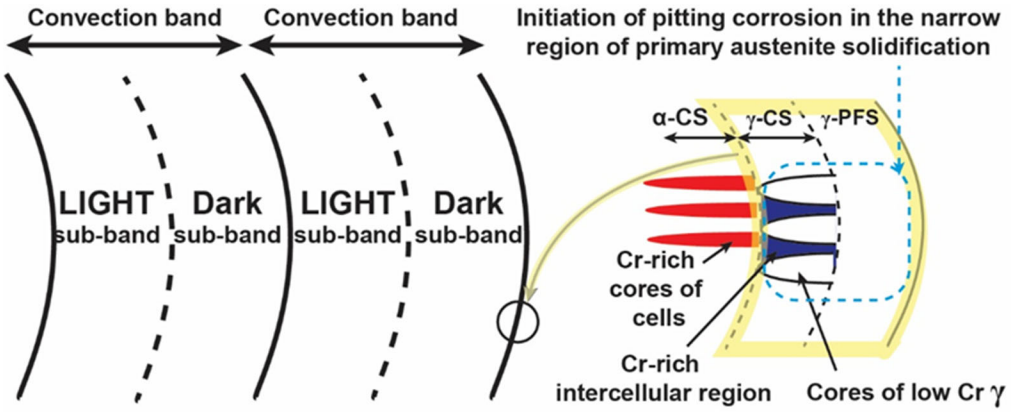

Figure 7. Sketch of the convection band's complete microstructure, as described in Appendix C. Pit initiation occurs in the narrow regions of primary austenite solidification, which are located along the outer edge of the convection bands. Pit initiation was not detected within the zones of primary ferrite solidification.

3.3. Cross-sectional Surface of Laser Melted 316L SS – Propagation of Localized Corrosion

As shown in the SEM of Figure 8a, localized corrosion of the cross-sectional surface initiated at the interface between the Glyptal paint mask and the sample. The sizes of the sites of localized corrosion are very different on the top surface and cross-sectional surface. As already discussed in the preceding subsection, on the top surface a large number of relatively small pits form along the outer edges of convection bands. In contrast, the localized corrosion of the cross-sectional surface consists of a few, relatively large regions of crevice corrosion.

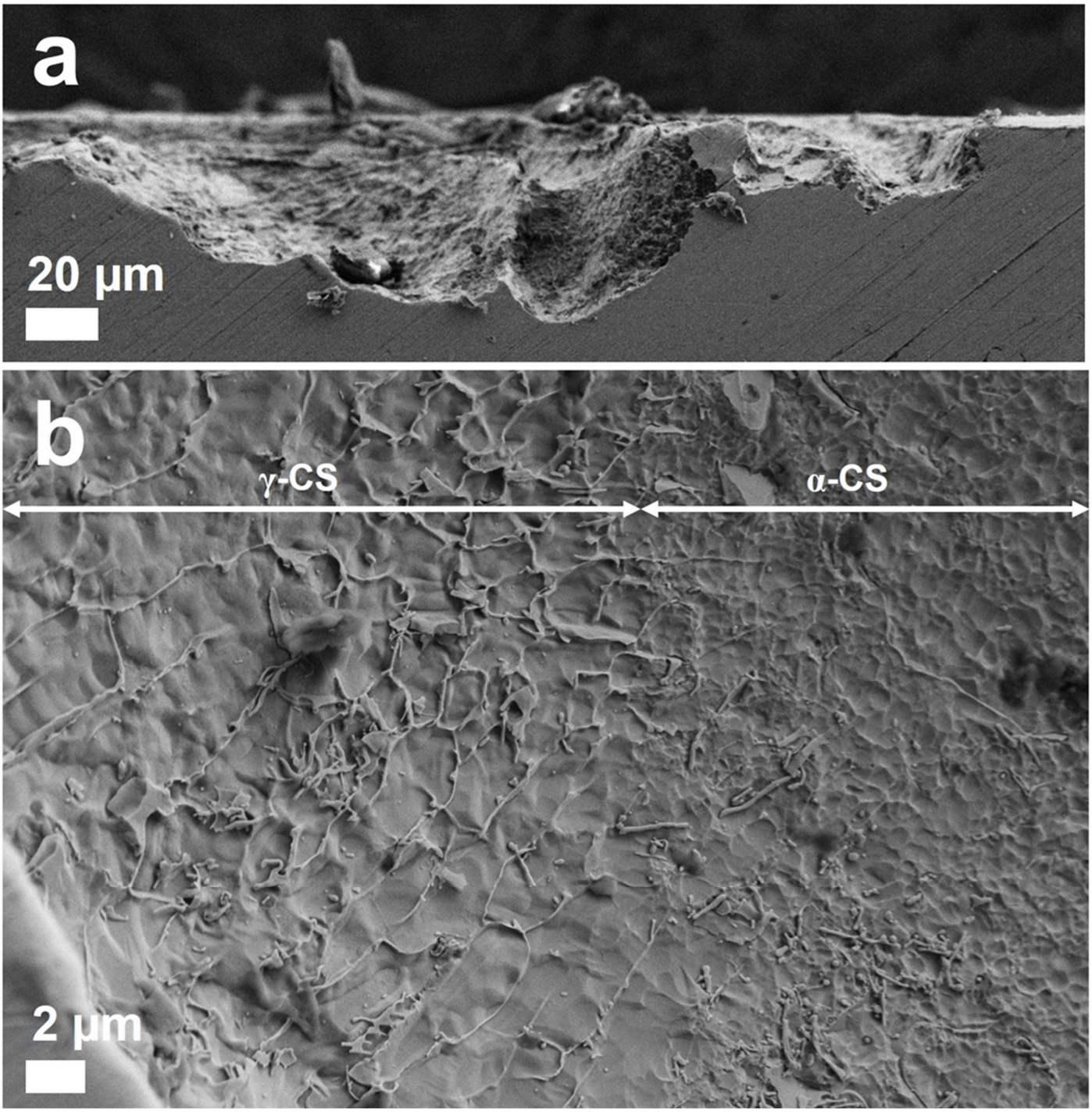

Figure 8. (a) Scanning electron micrograph of cross-section of the LSM 316L SS after anodic polarization in 0.1M HCl. Crevice corrosion occurs at the junction of the sample with the plastic sample mount. (b) Scanning electron micrograph of the crevice corroded surface. Along the outer edge (left-hand side of micrograph) the mode of solidification is γ -PFS, which results in preferential corrosion of the chromium-depleted interiors of the cells and places the chromium-rich intercellular spaces in relief. On the right-hand side the mode of solidification has changed to α -CS.

The morphology of the interior surface of the crevice corrosion shown in Figure 8 is revealed by the higher magnification micrograph presented in Figure 8b. At the outer edge of the crevice corroded region (left-hand side of Figure 8b) the interiors of the solidification cells are more strongly attacked leaving the cell boundaries raised in relief. The surface morphology suggests the mode of solidification along the perimeter of the crevice corroded region is γ-CS. We learned from metallography of the top surface that γ-CS is the mode of solidification along the outer edge of the convection band. Thus, the perimeter of the site of crevice corrosion pictured in Figure 8 occurs along the outer edge of the convection band, but we believe this is coincidental.

For clarification, in our view there is no specific reason why crevice corrosion would stop at the edge of a convection band as it has in Figure 8(a, b). In fact, the volume of each site of crevice corrosion is relatively large, indicating that the crevice corrosion has propagated through a number of convection bands. The main conclusion of the surface morphology is that within the occluded volume of the crevice the rate of corrosion of the chromium-depleted austenitic cores is greater than the rate of corrosion of the chromium-enriched cell boundaries.

As summarized in the sketch presented in Figure 7, further in from the edge of the convection band the primary phase of solidification changes to ferrite. As indicated in Appendix C.1, the transition from primary austenite to primary ferrite occurs at a distance of approximately 10 microns from the outer edge of the convection band. At approximately the same distance of 10 μm from the edge of the crevice corrosion shown in Figure 8b the morphology of the crevice corroded surface changes. The change in surface morphology corresponds to the transition from γ-CS to α-CS.

The morphology of the corroded surface of α-CS, which is presented in the righthand side of Figure 8b, suggests that unlike the case of γ-CS, there is not a significant difference in the amount of corrosion of the primary ferrite cell's interior and boundary. The morphology of the crevice corroded surface along with the previously-mentioned absence of pit initiation in the regions of α-CS suggest that the lower chromium concentration of the cell boundary is high enough to provide corrosion resistance equivalent to that of the cell's core. The higher chromium concentration of the primary ferrite cells is a consequence of the fact that chromium's equilibrium partition coefficient is greater than 1 for the ferrite phase.[11], [12] It is also possible that the distribution of chromium within the primary ferrite cell is homogenized as a consequence of the high solute diffusivity of the body-centered-cubic crystal structure.

3.4. Summary of Microstructure and Localized Corrosion

Our results indicate that the mode of solidification and the primary phase of solidification, which are sketched in Figure 9 along with information about the spatial extent of each zone of solidification, strongly affect the initiation of localized corrosion. Specifically, on the top surface of ground and polished, LSM 316L SS pits preferentially initiate along the outer edge of the convection band, which is the region of transient solidification, and which is composed of the low chromium, primary austenite zones of plane front solidification and cellular solidification. Since molybdenum is also a ferrite stabilizer like chromium it is possible that the austenitic region is also depleted in molybdenum and that the combination of chromium and molybdenum depletion is responsible for the nucleation of pits in the primary austenitic regions along the outer edge of the convection bands.

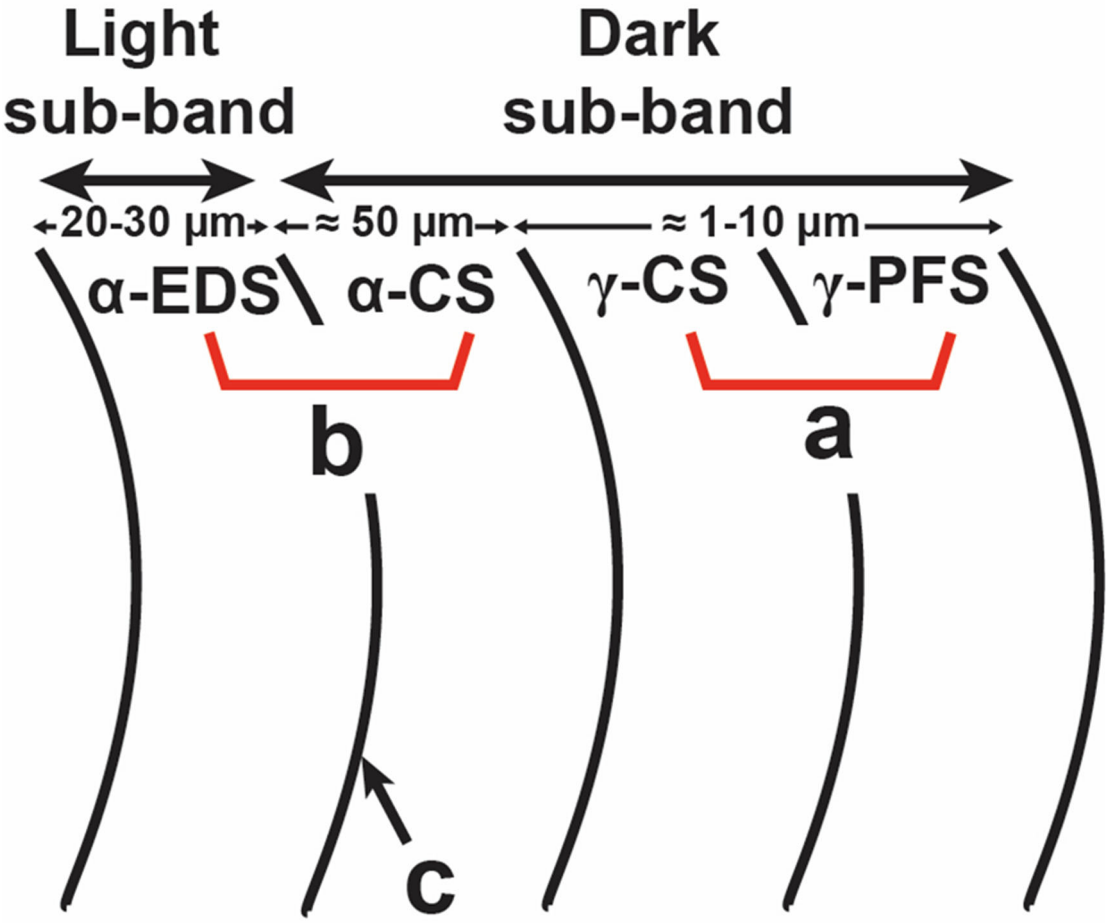

Figure 9. Summary of the effect of local processing conditions on microstructure of LSM 316L SS. (a) Primary γ is the result of locally high cooling rate and large undercooling associated with the outer edge of the convection band. (a and b) The transition from primary γ to primary α is driven by the low undercooling associated with higher laser power density of ≈ 10-18 MW/cm^2 at steady state. (c) The transition from α-CS to α-EDS is caused by high convection created within the liquid by high recoil pressure and the Marangoni effect.

The sites of crevice corrosion, which occurs during anodic polarization of the cross-sectional surface, are much larger than the pits formed during anodic polarization of the top surface and the volume of each site of crevice corrosion is composed of multiple convection bands. The surface morphology of one site of crevice corrosion reveals the primary austenitic mode of solidification along the bottom of the laser remelted volume and the primary ferritic mode of solidification within the interior of the laser remelted volume.

It is noteworthy that localized corrosion is not initiated in the region of primary ferrite solidification. Thus, our results indicate the steady-state solidification structure (i.e., primary ferritic, cellular solidification) is more resistant to pitting corrosion than is the narrow zone of the initial, transient solidification of γ-PFS and γ-CS. That is, the increased susceptibility to pitting corrosion of LSM 316L SS is attributed to the transient stage of solidification in which the first phase to freeze is the low-chromium-containing metastable austenite.

4. DISCUSSION

It is instructive to compare the present results with the results of several earlier studies of the pitting resistance of wrought and rapidly solidified (AM and LSM) 316L. Previous studies indicate two aspects of microstructure of 300 grade stainless steels that affect resistance to pitting corrosion: (1) inclusions and (2) phase transformations that cause local changes in concentrations of chromium and molybdenum.

First, consider inclusions. MnS inclusions are known to preferentially initiate pits in wrought 300 grade stainless steels.[19], [20] In some studies in which AM exhibits greater resistance to pitting than the wrought material, the superior resistance of AM is correlated with the absence or reduced size of MnS inclusions. For example, Stewart and Williams[21] report that LSM increased the pitting resistance of 304L in dilute neutral chloride by markedly decreasing the size of sulfur-containing inclusions. Sander et al.[22] find that the pitting potential of Laser Powder Bed Fusion (AM-LPBF) 316L is greater than that of wrought 316L in 0.1M NaCl and they suggest the greater pit resistance of AM is a consequence of the absence of, or reduced size of MnS inclusions. In a closely similar conclusion, Chao et al.[23] determine that the higher pitting potential of AM-LPBF 316L in 0.6M NaCl (approximately 0.5V higher) compared to that of wrought 316L is a consequence of the complete absence of MnS inclusions in the AM microstructure.

In contrast to the results of Stewart and Williams and of Sander et al., Ganesh et al.[24] and Trelewicz et al.[25] indicate the pitting resistances of AM-Directed Energy Deposition(DED) and AM-LPBF, respectively, are less than that of wrought 316L in 3.5% NaCl and in 0.1M HCl, respectively. In both cases the lower pit resistance of AM is attributed to phase transformations that create localized regions of low chromium and low molybdenum concentrations. Relatively low magnification optical microscopy in Ganesh et al. indicates that in relatively large diameter pits (i.e., 20-30 μm) the cores of primary austenite cells are preferentially corroded, and the cell boundaries are uncorroded. In addition, the γ– χ grain boundaries are also preferentially pitted due to sensitization. Solution annealing (SA) healed the chromium depleted zones of the sensitized grain boundaries so that pits did not form along γ–γ grain boundaries. SA did not homogenize the Cr concentration of the primary austenite cells so that within the pits the cell cores were preferentially corroded, and the cell boundaries were uncorroded as is the case for the as-LSM samples.

In instances of primary ferritic AM Ganesh et al found that pits preferentially formed along austenite-ferrite boundaries, which they suggested is due to segregation of sulfur and phosphorus, and along sensitized γ–γ grain boundaries. As was the case for primary austenite AM, SA removed the Cr-depletion along γ–γ grain boundaries so that pitting did not occur along γ–γ grain boundaries of SA primary ferritic. Trelewicz et al does not include a microscopic examination of the surfaces of pitted samples. But their microchemical analyses indicate that molybdenum preferentially segregates to the cell boundaries of primary austenite and they suggest that the lower pitting resistance of AM is a consequence of low molybdenum concentration of the cores of primary austenite cells.

Finally, it is worth mentioning several additional comparative studies if only because they provide further evidence of the wide variation in the relative resistances to pitting corrosion of wrought and rapidly solidified (i.e., AM and LSM) 316L. Lohdi et al.[26] find AM exhibits greater pitting resistance than wrought 316L in 0.9% NaCl, but in two other studies conducted in the same electrolyte Sun et al.[27] and Zietala et al.[28] indicate that AM-DED 316L has lower pitting resistance than wrought 316L on account of porosity and because of chromium segregation, respectively. Majumdar et al.[29] measure the pitting potential of AM-DED cladding of 316L in 3.56% NaCl to be 125 mV higher than that of wrought 316L. Lohdi et al.[26] and Majumdar et al. [29 do not identify the initiation sites of

pitting and the morphology of corroded pits. Lohdi et al.[30] find that neither AM nor wrought 316L pit during potentiodynamic polarization in acidic solutions (pH 1-3) with dilute concentration of chloride (≈0.01 M).

Thus, our results, which indicate the pit resistance of LSM 316L is less than that of wrought 316L and indicate the lower pitting potentials of AM is due to the formation of very narrow regions of primary austenite, are consistent with the results of Ganesh et al and Trelewicz et al., which also found or suggested corrosion preferentially occurs in low Cr regions, i.e., cores of primary austenite as well as along sensitized γ–γ grain boundaries of AM.

Therefore, our results in combination with earlier investigations of the comparative pitting corrosion of wrought and rapidly solidified (AM and LSM) 316L indicate that in those cases in which rapidly solidified 316L has greater resistance to pitting than wrought 316L, the greater resistance is attributed to the absence of or reduced size of MnS. And, in those cases in which rapid solidification exhibits less resistance to pitting than wrought, the lower resistance is due to the presence in the rapidly solidified microstructure of chromium depleted zones, e.g., the chromium depletion associated with sensitization and with the low chromium concentrations of cores of primary austenite cells.

5. CONCLUSIONS

- On ground and polished surfaces of laser surface melted 316L SS pitting corrosion preferentially initiates at convection bands that are created by a combination of the Marangoni effect and a high recoil pressure.
  - Within the convection bands the mode of solidification changes with increasing distance from the outer edge. γ- PFS occurs along the extreme outer edge and changes to γ- CS, and then to two regions of primary ferrite solidification: α-CS followed by α-equiaxed dendritic solidification (EDS).
  - Pits initiate in the regions of primary austenite solidification along the outer edge of the convection band. Specifically, the nucleation of pitting corrosion occurs in the very narrow region of transient solidification along the edges of the convection bands. The steady-state microstructure of 316L SS consists of α-CS and α-EDS and is more resistant to pit initiation than is the transient γ-PFS and γ-CS.
- Sites of crevice corrosion created during anodic polarization of the cross-sectional surface grow through multiple convection bands. The morphology of the surface of crevice corrosion indicates preferential corrosion of the chromium-depleted austenitic cores of the solidification cells, which places the chromium-rich intercellular regions in positive relief. The morphology of the surfaces of crevice corrosion of the region of α-CS solidification indicate there is no significant difference in corrosion attack of the cell's cores and the cell boundaries of α–CS, which is the steady-state mode of solidification of 316L SS.
- Anodic polarization in aqueous 0.1M HCl of unpolished, as-laser-melted surfaces indicates that the high laser power employed (≈10-18MW/cm^2 absorbed power density and ≈ 22-38 MJ/cm linear energy density) creates metal droplets on the free surface that nucleate pitting corrosion.
- The combination of the present results and the results of earlier studies suggests that instances in which rapidly solidified 316L exhibits greater susceptibility to pitting corrosion than wrought 316L are a consequence of phase transformations (sensitization and solidification) that create local regions of chromium-depleted zones in the rapidly solidified microstructure, And, in cases in which rapidly solidified 316L exhibits greater resistance to pitting corrosion than wrought 316L, the rapidly solidified microstructure is free of local regions of chromium depletion and is either free of MnS inclusions or contains MnS inclusions that are very small and below the critical size required to initiate stable corrosion pits.

REFERENCES

[1] Y. Hwa, C. S. Kumai, T.M. Devine, N. Yang, J.K. Yee, R. Hardwick and K. Burgmann, *Journal of Materials Science and Technology*, 69 (2020): p. 96-105.

[2] W. E. King, A. T. Anderson, R. M. Ferencz, N. E. Hodge, C. Kamath, S. A. Khairallah, and A. M. Rubenchik, Applied Physics Reviews 2, (2015) p. 041304.

[3] S. Gorsse, C. Hutchinson, M. Goune, and R. Banerjee, Science and Technology of Advanced Materials, 18, (2017) p. 584-610.

[4] T. DebRoy, H.L. Wei, J.S. Zuback, T. Mukherjee, J.W. Elmer, J.O. Milewski, A.M. Beese, A. Wilson-Heid, A. De, W. Zhang, *Progress in Materials Science*, 92, (2018) 112-224

[5] P. A. Khan and T. DebRoy, *Metallurgical Transactions B*, 15B, (1984) p. 641-644.

[6] K. Mundra and T. DebRoy, Metallurgical Transactions B, 24B, (1993) p. 145-155.

[7] S. A. Khairallah,* A. T. Anderson, A. Rubenchik, W. E. King, *Acta Materialia*, 108 (2016) p. 36-45.

[8] G. Sander, J. Tan, P. Balan, O. Gharbi, D. R. Feenstra, L. Singer, S. Thomas, R.G. Kelly, J. R. Scully, and N. Birbilis, *Corrosion*, 74, (2018) p. 1318-1350.

[9] T. Mukherjee, H. L. Wei, A. De, T. DebRoy, *Computational Materials Science*, 150 (2018) p. 369-380.

[10]N. A. Kistler, A. R. Nassar, E. W. Reutzel, D. J. Corbin, A. M. beewse, *Journal of Laser applications*, 29, (2017) p. 022005-1–12.

[11]S. A. David, J. M. Vitek, R. W. Reed, and T. L. Hebble, *Oak Ridge National Laboratory Report*, (1987) ORNL/TM-10487.

[12]S.A. David, J. M. Vitek, T. L. Hebble, *Welding Journal*, *Welding Research Supplement*, (1987) p. 289s-300.

[13]C. Wu, S. Li, C. Zhang, X. Wang, *Journal of Materials Science*, 51, (2016) p. 2529-2539.

[14] U. S. Bertoli, B. E. Macdonald, J. M. Schoenung, *Materials Science and Engineering A*. 739 (2019) p. 109–117.

[15] T. Pinomaa, M. Lindroos, M. Walbruhl, N. Provatas, S. Laukkanen, *Acta Materialia* 184 (2020) p. 1-16 (2020).

[16] N. J. Harrison, I. Todd, K. Mumtaz, *Acta Materialia* 94 (2015) p. 59-68.

[17] X. Zhao, J. Chen, X. Lin, W. Huang, *Materials Science & Engineering. A* 478 (2008) p. 119-124.

[18] F. Liu, X. Lin, G. Yang, M. Song, J. Chen, W. Huang, *Optics & Laser Technology* 43 (2011) p. 208-213.

[19]G. S. Eklund, *Journal of the Electrochemical Society*, 121, (1974) p. 467.

[20]G. Wranglen, *Corrosion Science*, 14 (1974) p. 331-349.

[21]J. Stewart and D.E. Williams, *Corrosion Science*, 33, (1992) p. 457-474.

[22]G. Sander, S. Thomas, V. Cruz, M. Jurg, N. Birbilis, X. Gao, M. Brameld, and C. R. Hutchinson, *Journal of the Electrochemical Society*,164 (2017) p.C250-C257.

[23]Q. Chao, V. Cruz, S. Thomas, N. Birbilis, P. Collins, A. Taylor, P. D. Hodgson, D. Fabijanic, *Scripta Materialia*, 141 (2017) p. 94-98.

[24]P. Ganesh, R. Giri , R. Kaul, P. R. Sankar, P. Tiwari, A. Atulkar, R. K. Porwal, R. K. Dayal, L. M. Kukreja, *Materials and Design*, 39 (2012) p. 509-521.

[25]J. R. Trelewicz, G. P. Halada, O. K. Donalldson, G. Manogharan, *Journal of Metals*, 68, (2016) p. 850-859.

[26]M. J. K. Lodhi, K. M. Deen, M. C. Greenlee-Wacker, W. Haider, *Additive Manufacturing*, 27 (2019) p. 1-19.

[27]Y. Sun, A. Moroz, and K. Airbaey, *Journal of Materials Engineering and Performance*, 23, (2014) p. 518-526.

[28]M. Ziętala, T. Durejko, M. Polański, I. Kunce, T. Płociński, W. Zieliński, M. Łazińska, W. Stępniowski, T. Czujko, K. J. Kurzydłowski, Z. Bojar, *Materials Science & Engineering A*, 677, (2016) p. 1-10.

[29]J. D. Majumdar, A. Pinkerton, Z. Liuy, I. Manna, L. Li, *Applied Surface Science*, 247, (2005) p. 373-377.

[30]M. J. K. Lodhi, K. M. Deen, W. Haider, *Materialia*, 2 (2018) p. 111-121

APPENDIX A. PREFERENTIAL ETCHING OF CHROMIUM-RICH REGIONS

In this investigation etching is conducted potentiostatically in concentrated nitric acid at an applied potential of +0.8 V vs RHE. The following results demonstrate that our etching procedure preferentially attacks chromium-rich regions. Anodic polarization curves were measured of three binary iron-chromium alloys: Fe-5w/oCr, Fe-10w/o Cr, and Fe-13 w/o Cr as well as of Fe-5 w/o Cr – 10 w/o. Each of the four alloys is cast in vacuum as a 19 lb. cylinder, followed by hot and cold working into 1.52 mm diameter wires. Each sample of the anodic polarization test is approximately 40 mm in length. Each test is conducted in approximately 500 cc of air-saturated, concentrated nitric acid (65 w/o). Platinum mesh is the counter electrode, and a 2 mm diameter platinum wire serves as a pseudo reference electrode. The potential of the platinum pseudo-reference electrode in air-saturated concentrated nitric acid is +1.108 V with respect to the saturated calomel electrode. Each sample is anodically polarized at a rate of 1 mV/s.

The anodic polarization curves of the four alloys are presented in Figure A-1. The sharp increase of oxidation rate in the anodic polarization curves at potentials of approximately +0.45V, +0.60V and +0.65V with respect to the platinum pseudo-reference for Fe-13Cr, Fe-10Cr and Fe-5Cr, respectively, is the result of oxidative dissolution of Cr_2O_3 to hexavalent chromium. The polarization behavior of Fe-5Cr-10Ni indicates that 10 w/o Ni does not have a significant effect on the potential at which Cr_2O_3 is oxidatively dissolved.

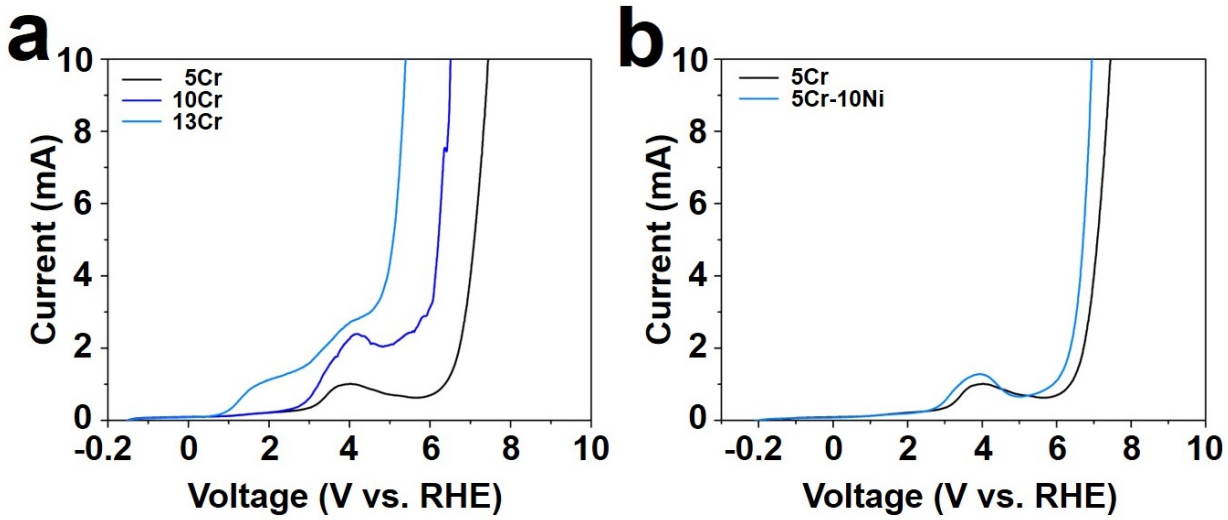

Figure A-1. (a) Anodic polarization curves in air-saturated, concentrated nitric acid of three binary iron-chromium alloys (Fe-5w/o Cr, Fe-10 w/o and Fe 13 w/o Cr) and (b) one ternary alloy (Fe-5 w/o Cr – 10 w/o Ni).

The results presented in Figure A-2(a-d) confirm that our etching practice preferentially attacks chromium rich regions. In the cellularly solidified portion of the laser remelt track of 316L SS (Figure A-2a), which is formed with a power density of 200W and a translation speed of 4.3 mm/s, the etching procedure preferentially attacks the intercellular regions, which the elemental maps of nickel, molybdenum and chromium (Figures A-2b, c, d) and the quantitative analyses of the intercellular region (see Table A-1) indicate are chromium rich.

Table A-1. Quantitative Analysis of Cr, Ni, Fe, and Mo in the intercellular region and in the region with the core of the cell as identified in Figure A-2b.

	Cr (at.%)	Ni (at.%)	Fe (at.%)	Mo (at.%)
Area 1	17.3	11.8	69.5	1.4
Area 2	20.9	8.1	69.0	2

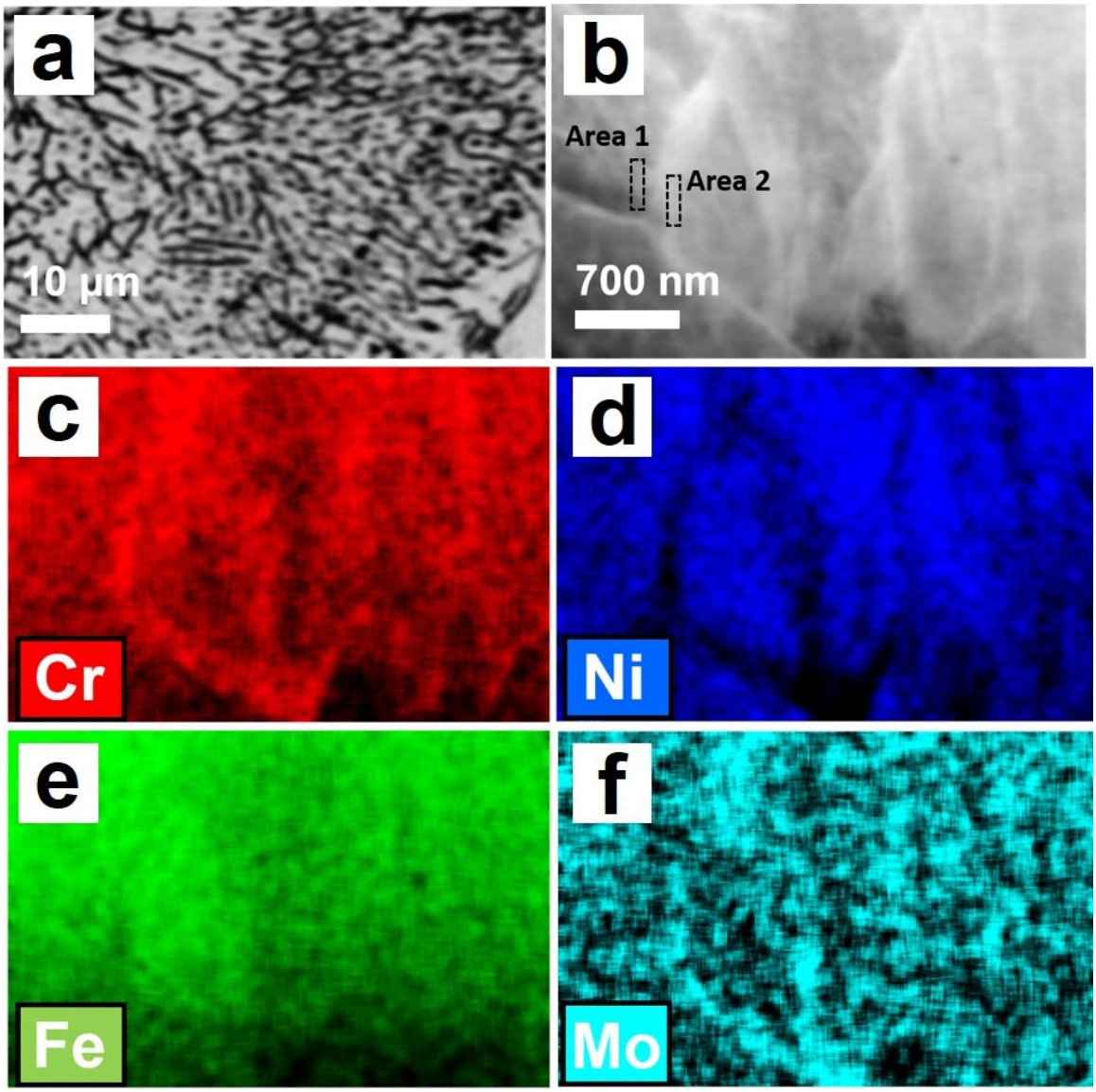

FIGURE A-2. Cellular solidification of LM Track H. (a) High magnification optical micrograph of region of CS of Track H selected for HAADF. (b) HAADF-STEM image of the region of cellular solidification. (c) Elemental map of chromium distribution. Note chromium enrichment of intercellular region. (d) Elemental map of nickel distribution. Note nickel depletion of intercellular region. (e) Elemental map of iron distribution. (f) Elemental map of molybdenum distribution.

APPENDIX B. ANODIC POLARIZATION OF AS LASER-MELTED SURFACE

The anodic polarization curves of the as-received plate of 316L SS and of the as laser-remelted surface are presented in Figure B-1.

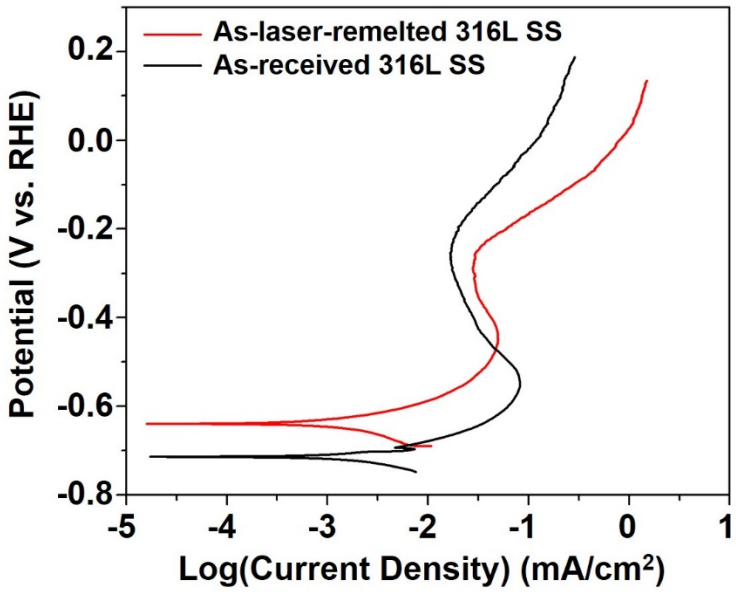

FIGURE B-1. Anodic polarization in 0.1 M HCl (saturated with $N_{2(g)}$) of as-received plate of 316L SS and of as-laser-remelted 316L SS.

The polarization curves of both the as-received plate and the as laser-remelted surface are similar. However, whereas the pits were randomly distributed on the surface of the as-received plate, the pits were preferentially located on the portion of each track that was immediately adjacent to the next-deposited track. As shown in Figure B-2a and explained by the sketch in Figure B-2b the pits occurred in the region of the track that was partially coated with molten-alloy droplets created by the recoil pressure[7].

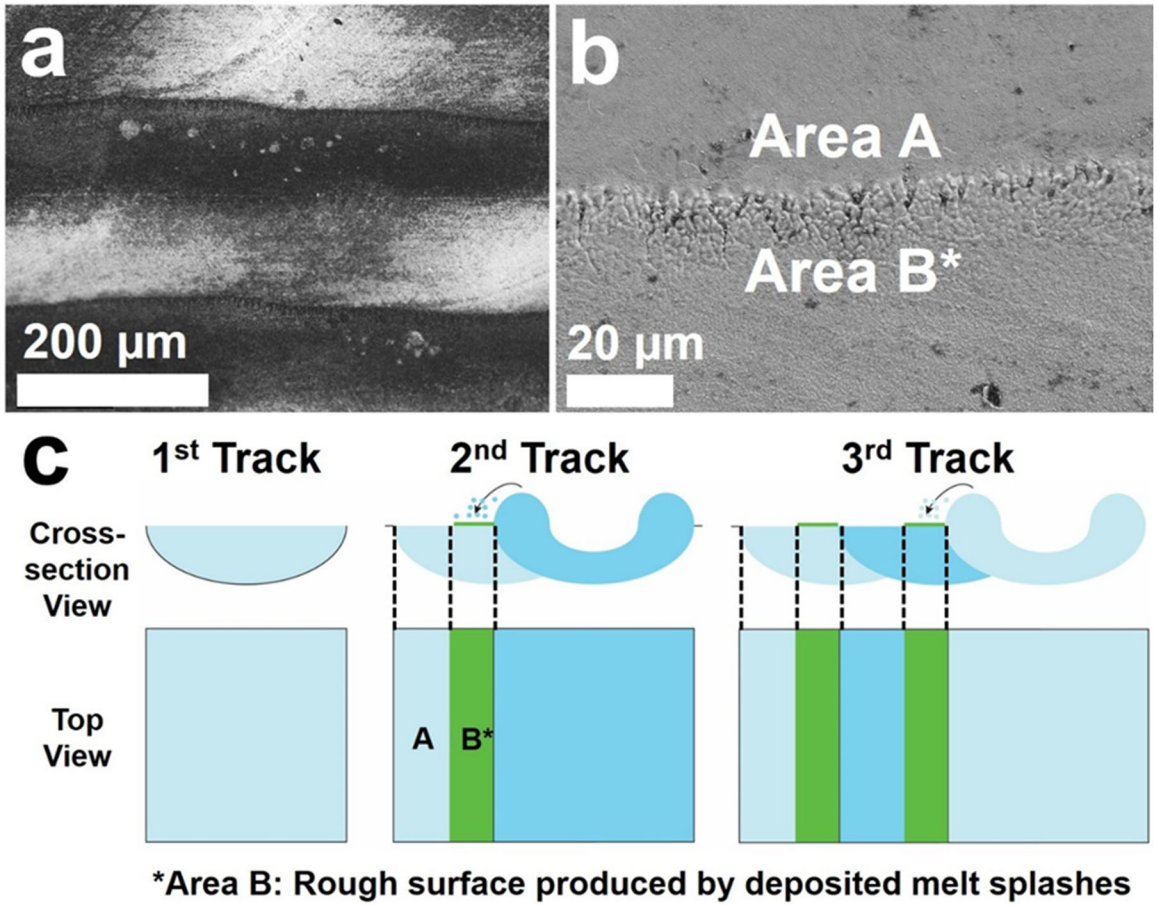

FIGURE B-2. (a) Top surface of as laser melted 316L SS following anodic polarization in 0.1M HCl. Pits nucleate on the portion of track adjacent to the next-deposited track. (b) Higher magnification SEM image of region of overlap of adjacent tracks after anodic polarization in 0.1M HCl. Surface of overlap is rough and pitted. (c) Schematic illustration: formation of the region partially coated with molten-alloy droplets.

EDS spectra indicated there are no significant differences in composition in the different regions of the track. A possible cause of the preferential pit location is initiation by underdeposit corrosion at the site of the metal droplets. Comparing the results of the as-received plate and the laser-remelted surface indicate that although there is no difference in the pitting potentials, there is a significant increase in the number of pits associated with the as-laser-remelted surface.

APPENDIX C. ENTIRE MICROSTRUCTURE OF A CONVECTION BAND – TRANSITION FROM PRIMARY FERRITE TO PRIMARY AUSTENITE

From the perspective of initiation of pitting corrosion, the most important microstructure is the two regions of primary austenite solidification (i.e., γ-PFS and γ-CS) that occur along the outer edge of the convection bands. A series of changes in microstructure occur beyond this region of primary γ solidification. We describe these changes for the sake of completeness, but the results and discussion are presented in this appendix rather than in the body of the paper because these changes do not affect the initiation of localized corrosion. It is possible that these changes have an impact on other types of corrosion, such as environmentally assisted cracking.

Information about the influence of microstructure on the initiation of pitting corrosion is provided by searching for evidence of corrosion at increased distance from the edge of the convection band, which is where initiation occurs. Figure C-1(a, b, and c) present optical micrographs of a more heavily etched surface than that shown in Figure 7 and Figure 8. The relatively low magnification of the micrographs in Figures C-1(a and b) reveal the cyclic changes in microstructure associated with the convection bands. Note that each convection band is composed of two sub-bands, e.g., A and B, and C and D. One sub-band (e.g., A and C) is darker as a consequence of more etchable features. The other sub-band has few etchable features and is light colored (e.g., B and D). The microstructure along the outer edge of the sub-bands A and C is not resolvable given the low magnification of the optical micrographs but consists of the narrow regions of γ-PFS and γ-CS shown in Figure C-1

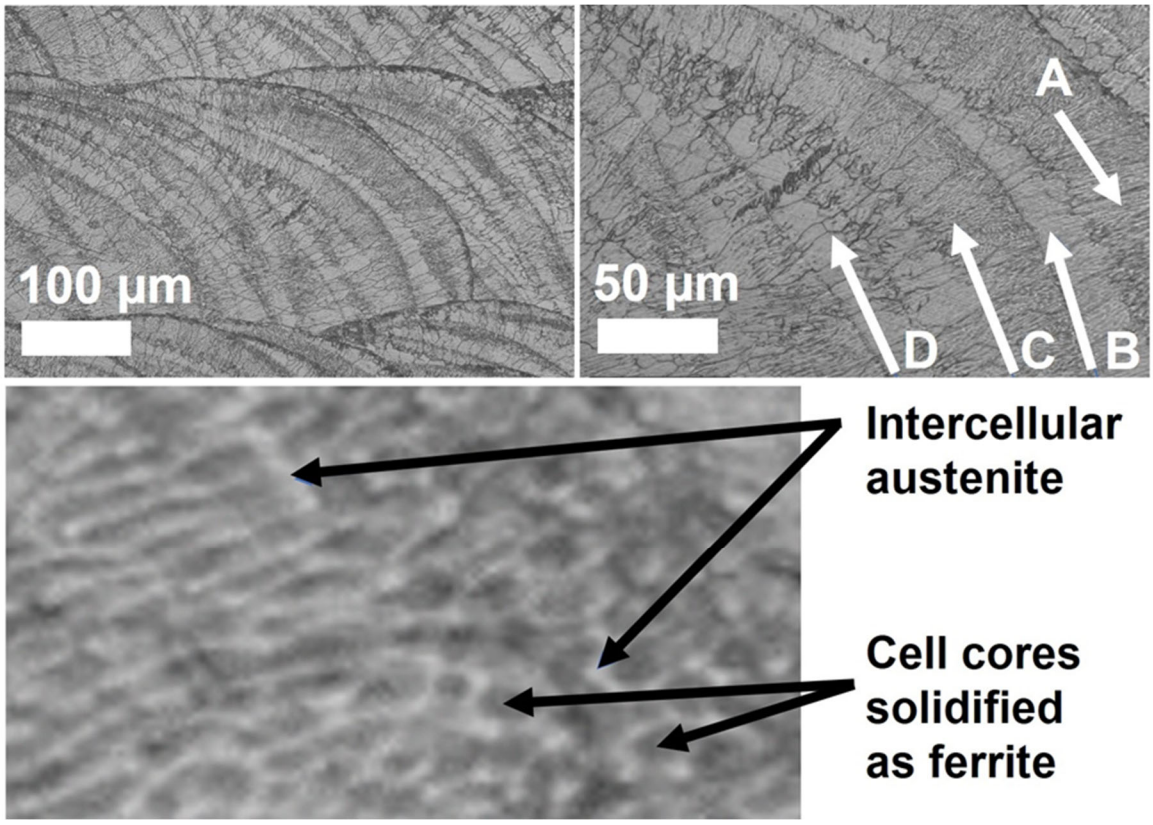

FIGURE C-1. Optical micrographs of ground and polished top surface of laser melted 316L SS after significant etching. (a) The top surface is composed of partially overlapping, laser surface melted tracks. (b) The direction of solidification is approximately from the upper righthand corner to the lower left-hand corner. The microstructure consists of alternating sub-bands of dark (A and C) and light (B and D) etching. The two zones of primary austenite solidification, γ-PFS and γ-CS, occur along the outer edge of the convection band (i.e., junction of B and C) but are narrow and not resolvable. Primary ferrite, cellular solidification (α-CS) is the mode of solidification of the darkly etched sub-bands, A and C, which are 30-50 µm wide. The mode of solidification within the lightly etched sub-bands, B and D, which are approximately 20 µm wide, is equiaxed dendritic (ED). (c) The more lightly etched regions are bright and in relief and are austenitic. They are nearly continuous and form the cell boundaries. The more heavily etched regions solidified as ferrite and form the cores of the cells.

The vast majority of sub-bands A and C is composed of α-CS as is apparent in the magnified image in Figure C-1c. The cell boundaries and the cells' cores are identified in Figure C-1c. The solidification microstructure is identified as α-CS on account of (1) the continuous, lightly etched regions that are in relief, and (2) the deeper attack of the island-like regions. The continuous regions form the cell boundaries, and the island-like regions form the cores of the cells. The deeper attack of the cores indicates the cores have a relatively high chromium concentration and, therefore, solidified as ferrite. The lighter attack of the cell boundaries indicates a relatively low chromium concentration.

The change in the primary phase of solidification from austenite to ferrite at a distance of 10 µm from the outer edge of the convection band (i.e., the outer edge of sub-band A) is a consequence of the following: (i) once quasi steady-state solidification is reached the undercooling associated with a high laser power such as 200W is relatively small, and (ii) low undercooling promotes freezing of the thermodynamically stable phase, which is ferrite for 316L SS.

The boundary between the dark sub-band and the light sub-band occurs at a distance of approximately 50 μm from the edge of the convection band and marks a change in the mode of solidification from α-CS to α-ED (equiaxed dendritic) (See Appendix C.1).

It is worth noting that the light sub bands are not sites of initiation of pitting. Although there is no effect of the light sub bands on pitting, which is the primary focus of this paper, the different microstructure of the light sub band might affect resistance to EAC and so this microstructure is further discussed in Appendix C.1.

The influence of microstructure on the localized corrosion is summarized in the sketch presented in Figure 9 in the body of the paper.

C.1. Entire Microstructure of a Convection Band – Transition from Cellular (dark sub-bands) to Equiaxed Dendritic (light sub-bands) Solidification

The cross-section of the laser-surface melted track formed with a laser power of 375W and a translation speed of 25 mm/s is presented in Figure C-2. A narrow band of plane front solidification is present at the interface of the deposit and the substrate. Approximately five microns from the interface with the substrate the mode of solidification changes to cellular. The chromium-rich regions are preferentially etched and form the cells' boundaries, which indicates austenite (fcc) is the primary phase of solidification. As distance from the substrate increases the mode of solidification changes from cellular to equiaxed-dendritic. The region of equiaxed grains is associated with high laser power, which creates a high recoil pressure. The high recoil pressure induces significant convection of the melt pool. The high convection breaks off pieces of cells that then serve as nuclei of solidification. The transition from cellular solidification to equiaxed dendritic solidification occurs along a very rough, irregularly shaped boundary.

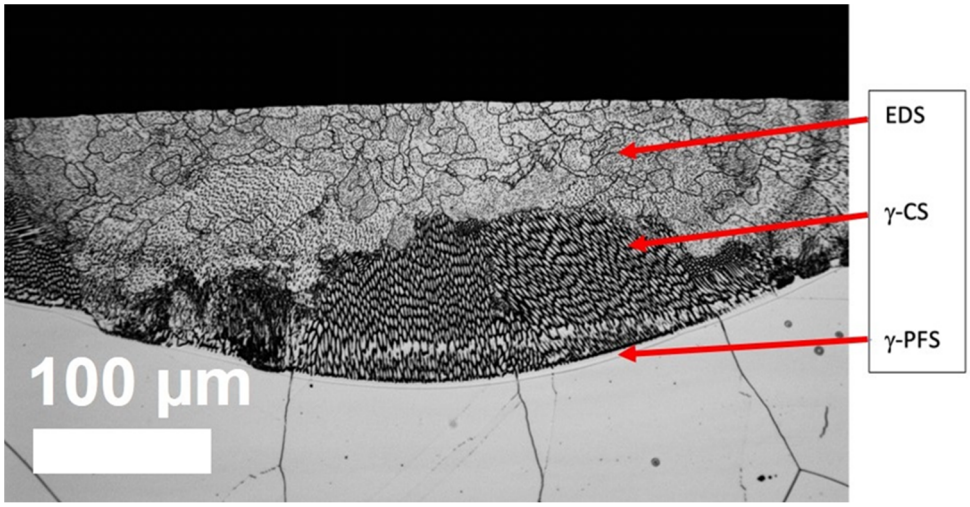

FIGURE C-2. Cross-section of laser surface melted track of 316L SS formed with a laser power of 375 W and a translation speed of 10 mm/s

Refer once again to the micrograph that is presented in Figure B-1. Note the irregular shape of the sharp interface between the regions of α-CS and α-EDS. The EDS zone labeled "D" is wider than the others that are shown and contains two layers of grains. It is also worth noting that the nitric acid etch indicates there is less variation in chromium concentration between the cores and the interdendritic spaces. In other words, the chromium concentration is more uniform, which might account for the absence of initiation of pitting corrosion in the α-EDS regions.

DISTRIBUTION

Email—Internal

Name	Org.	Sandia Email Address
Josh Yee	8246	jkyee@sandia.gov
Cristina Martinez	8246	cmarti@sandia.gov
Paul Spence	8240	paspenc@sandia.gov
Mike Hardwick	8200	mfhardw@sandia.gov
Nancy Yang	8341	nyyang@sandia.gov
Rick Karnesky	8341	rakarne@sandia.gov
Christian Mailhiot	8340	cmailhi@sandia.gov
Technical Library	01977	sanddocs@sandia.gov

Email—External

Name	Company Email Address	Company Name
Yoon Hwa	Yoon.hwa@asu.edu	Arizona State University
Christopher Kumai	ckumai@berkeley.edu	University of California, Berkeley
Tom Devine	devine@berkeley.edu	University of California, Berkeley

Sandia National Laboratories

Sandia National Laboratories is a multimission laboratory managed and operated by National Technology & Engineering Solutions of Sandia LLC, a wholly owned subsidiary of Honeywell International Inc. for the U.S. Department of Energy's National Nuclear Security Administration under contract DE-NA0003525.